



Mathematical modeling of catalytic wet oxidation in trickle-bed reactors by a diffusion–convection–reaction approach embedded with an interstitial CFD framework

Rodrigo J.G. Lopes*, M.L.N. Perdigoto, Rosa M. Quinta-Ferreira

CIEPQPF – Centro de Investigação em Engenharia dos Processos Químicos e Produtos da Floresta, GERSE – Group on Environmental, Reaction and Separation Engineering, Department of Chemical Engineering, University of Coimbra Rua Sílvio Lima, Polo II – Pinhal de Marrocos, 3030-790 Coimbra, Portugal

ARTICLE INFO

Article history:

Received 23 August 2010

Received in revised form 15 November 2011

Accepted 27 November 2011

Available online 3 December 2011

Keywords:

Computational fluid dynamics

Trickle-bed reactor

Multiphase flow

Catalytic wet oxidation

Total organic carbon

Temperature

ABSTRACT

In this work, we propose a diffusion–convection–reaction methodology to gain further insights into the heterogeneous multiphase flow of trickle beds. Our case-study encompasses a multi-fluid model embedded within an interstitial framework on the numerical simulation of continuous catalytic wet oxidation of hazardous compounds. First, with the proviso that phase holdup, pressure drop, and liquid distribution are fundamental criteria for the efficient design of trickle beds, the multiphase flow constitutive equations have been developed and solved by the conservative unstructured finite volume method. Second, several numerical variables were parametrically optimized based on the application of different under-relaxation parameters, mesh densities, and time stepping strategies. The segregated solver has been found to reveal good properties in terms of convergence and stability criteria, which endorsed the further corroboration. Finally, this theoretical probing-sensing scheme enabled the characterization of liquid flow texture accomplished by three-dimensional flow patterns exposing their deviation from ideal plug flow. The diffusion–convection–reaction framework coupled within a CFD model can then be further exploited on the simulation of complex multiphase reactive flows with adjustable parameters.

© 2011 Elsevier Inc. All rights reserved.

1. Introduction

In the realm of mathematical modeling of engineering and environmental processes, several on-going research activities focus on how to provide consistent remediation technologies of contaminated air, soil and water. Having realized that safer and cleaner processes are required to eliminate or at least minimize the effect of risky compounds on the environment, multiphase reactors are facing new challenges to detoxify gas and liquid polluted streams. In this regard, trickle-bed reactors have been envisaged as an effective path to manage toxic and hazardous liquid effluents without resembling a perennial problem which typically characterizes old-fashioned mineralization technologies. These wastewaters streams can be suitably dealt with by means of sub-critical solid-catalyzed wet oxidation (CWO) [1].

Trickle beds involve a multitude of subjects including heat transfer, fluid mechanics, and transport phenomena. Indeed, liquid-phase oxidation processes fall into the category of gas–liquid–solid reactions and are still not at a mature stage of development and technological implementation. As the overall outcome depends on their complex design and scheduling duties, this fact has been attributed to the multiphase character that poses many chemical reactor engineering challenges.

* Corresponding author. Tel.: +351 239798723; fax: +351 239798703.

E-mail address: rodrigo@eq.uc.pt (R.J.G. Lopes).

Nomenclature

$C_{\mu}, C_{1\varepsilon}, C_{2\varepsilon}$	k - ε model parameters: 0.09, 1.44, 1.92
C	specie concentration (ppm)
d_p	catalyst particle nominal diameter (m)
E_1, E_2	Ergun's constants: 180, 1.75
\vec{g}	gravitational acceleration (9.81 m/s ²)
G	gas mass flux (kg/m ² s)
G_{kL}	generation rate of turbulent kinetic energy
K_{pq}	interphase momentum exchange term
k	k - ε model kinetic energy
k'	apparent reaction rate constant
L	liquid mass flux (kg/m ² s)
p	pressure (bar)
$-r$	oxidation rate
$S_{q,i}$	source mass of specie i for phase q (ppm)
$S_{q,h}$	source term containing volumetric reaction heat (J)
t	time (s)
T	temperature (°C)
TOC	total organic carbon (ppm)
\vec{u}	superficial vector velocity (m/s)

Greek letters

α_q	volume fraction of q th phase
ε	k - ε model dissipation energy
ρ_q	density of q th phase (kg/m ³)
Δp	total pressure drop (Pa)
σ	surface tension coefficient
$\sigma_k, \sigma_\varepsilon$	k - ε model parameters: 1.2, 1.0
τ	residence time (s)
$\bar{\tau}_q$	viscous stress tensor of q th phase (Pa)
μ_q	viscosity of q th phase (Pa s)

Subscripts

G	gas phase
i	lumped specie
q	q th phase
L	liquid phase
S	solid phase

At this level, one can pinpoint a wide spectrum of issues that encompasses flow patterns and hydrodynamics, inter-phase and intra-particle heat and mass transport, kinetics and thermodynamics [2].

Despite the myriad of modeling and experimental studies being released in the academic and patent literature, there are too few industrially demonstrated applications of catalytic wet oxidation in trickle-bed reactors. Given the overwhelming progress in computer technology in recent years, here we investigate a theoretical framework based on advanced simulation CFD codes to gain further insights into trickle-bed reactors on the catalytic abatement of moderate- to high-strength wastewaters. As the operation of trickle beds are dictated by the nature of the hydrodynamic flow regime, one should pay particular attention to diffusion–convection–reaction models. Under trickling flow conditions, gas and liquid phases interact sluggishly so this low interaction regime is often described by low Peclet number and the pollutant diffusion transport cannot be neglected in such circumstances [3,4]. For such a multi-component system, the diffusion of liquid-dissolved contaminants should be accounted for and the multiphase flow governing equations are coupled and nonlinear second-order elliptic partial differential equations. The degree of coupling allows us to solve numerically those equations either in a segregated or non-segregated fashion. As a rule of thumb for concentrated multicomponent mixtures, segregation of the governing equations cannot be performed directly so the numerical strategy is performed by under-relaxation parameters to produce the system of equations amenable to numerical solution. On the contrary, in case of dilute mixtures there exists an opportunity to use a reference pollutant which constitutes most of the mixture and these equations become segregated or are only weakly coupled. In case of segregated frameworks, the self-diffusion operator is computed implicitly, while the diffusion due to the other pollutant species is treated explicitly. This fact results in an iterative algorithm whose convergence depends on the strategy used to conserve the overall mass constitutive equation.

In realization of the need to address numerically the modeling strategy, multiphase flow governing equations for a trickle bed case-study will be assessed on how the convergence criterion for the mass fraction balance can be imposed explicitly, and if the transport properties are not held constant, the convergence of this semi-implicit system of equations requires under-relaxation. As our case-study is devoted to the trickling flow regime which is mainly governed by the low interaction forces between the gas, liquid and solid phases, there exists within the individual flow channels or the so-called pores different local liquid-catalyst contacting characteristics. Therefore, the packed bed flow has to be directly simulated without implementing any averaging methodology for the mathematical domain in the CFD model except the numerical solution parameters so as to avoid any application of a further optimization *modus operandi*. Having considered a three-dimensional representation of the catalytic bed, the interstitial flow and the hydrodynamic/reaction parameters are directly computed by means of the numerical solution of mass, energy and momentum conservation equations.

The computational domain encompasses a multi-dimensional formulation, where the spatial operators have to be additionally split to enable use of iterative algorithm so the convergence will be guaranteed with optimum under-relaxation parameters. Given that the numerical approximation of advective terms can give rise to false diffusion errors on the decoupling of pressure and velocity variables in three-dimensional grids, flux discretization schemes should be used to circumvent cross-wind errors without sacrificing the scheme stability. Additionally, the divergence-free constraint condition for the velocity field in the simulation of incompressible Navier–Stokes equations is underpinned to avoid velocity and pressure oscillations without accuracy deterioration. During packed bed flow simulations, a mixed formulation for solving the multiphase flow equations is then implemented to conform with mass conservation balance. However, this methodology can lead to the conception of a less diagonally dominant coupled system of equations. The computation of primitive variables is then affected by the poor eigenvalue distribution and the increased sized of the resulting matrix. Therefore, the segregated algorithm can be applied to avoid the numerical issues that characterize the mixed formulation so the pressure scalar field (Poisson equation) is obtained independently from the velocity vector field by the solution of the momentum balance equation.

The present article is divided into three major parts: first, a brief literature survey is presented on specific cases of solution of the advection–diffusion–reaction equation. Secondly, the multiphase flow governing equations for a TBR under reactive flow conditions are detailed with the computational methodology used in the simulation procedure followed by the simulation setup and the relevant boundary conditions. Proceeding further, results are presented encompassing qualitative and quantitative comparisons of computed and experimental total organic carbon (TOC) concentration and temperature profiles. Convergence plots are discussed for several under-relaxation factors and various mesh size as well as different time steps. Finally, representative interstitial reaction flow maps of TOC and thermal silhouettes will be analysed by three-dimensional computational mappings.

2. Previous work

More than two decades have now passed since the publication of a robust method proposed by Patel et al. for reducing false-diffusion errors in convection–diffusion problems [5]. Although an upwind approximation which essentially follows the streamlines can be used to overcome those errors for finite difference-based methods it does have some shortcomings. The skew-upwind differencing scheme retains the general objectives of the Raithby approach, but uses an entirely different formulation that eliminates the shortcomings of the original scheme. The authors have demonstrated its performance on a standard test problem by comparing to other schemes and the results have shown an efficient minimization of false-diffusion in finite-difference based approaches. Similarly, Leonard has performed numerical studies to evaluate the order of accuracy of QUICK and related convection–diffusion schemes [6]. An alternative single-point upwind difference scheme using node values (with a 1/6-factor) was implemented by a third-order representation of the finite-difference single-point formulation and has been written in a pseudo-flux-difference form. The author has claimed that the QUICK finite-volume convection operator is 33% more accurate than the single-point implementation. After presenting also a single-point formulation of the convective derivative in terms of cell averages, finite-volume formulations was found to be significantly more accurate than finite-difference ones when diffusion operators are considered in both formulations. It was concluded that classical second-order central differencing for the second derivative is exactly twice as accurate in a finite-volume formulation as it is in a finite-difference formulation. A boundary element method analysis for the transient conduction–convection in 2-D with spatially variable convective velocity has been developed by DeSilva et al [7]. A time-dependent fundamental solution for a moving heat source with constant velocity was applied and numerical examples were included to establish the validity of the approach. The scheme has been found to avoid considerable false diffusion, and the numerical results for sample problems compared very well to analytical results. Recently, Zhan et al. investigated a high accuracy hybrid method for two-dimensional Navier–Stokes equations under high Reynolds and high Rayleigh number flows with a dual-mesh [8]. To combine the fast Poisson solver DFPS2H and the high-order upwind-biased finite-difference method on different meshes, Chebyshev polynomials have been used to transfer the data between the uniform and non-uniform meshes. They adopted successfully the hybrid grid system mainly due to the application of a fourth-order finite-difference scheme for the time-dependent convection and diffusion equations. It was found that the numerical model can handle the steep spatial gradients of the dependent variables by using very fine resolutions in the boundary layers at reasonable computational cost. A nonstandard technique for constructing *global a posteriori error estimates* for the stationary convection–reaction–diffusion

equation has been proposed by Korotov [9]. The underlying bilinear form was decomposed into several terms to estimate the approximation error in appropriate weighted energy norms. After introducing auxiliary parameters to construct such a splitting and tune the resulting upper error bound, this methodology was demonstrated on how those parameters can be chosen in some natural and convenient way for computations so that the weighted energy norm of the error is almost recovered. This procedure has been claimed to be completely independent of numerical techniques used to compute approximate solutions. Mohebbi et al. investigated high-order compact solution of the one-dimensional heat and advection-diffusion equations [10]. A compact finite difference approximation of fourth-order for discretizing spatial derivatives of these equations and the cubic C^1 -spline collocation method for the resulting linear system of ordinary differential equations have been applied for time integration of parabolic equations. The authors have shown that the proposed method is unconditionally stable and gives an efficient method for solving the one-dimensional heat and advection-diffusion equations.

The above-mentioned survey revealed that diffusion-convection models can be comprehensively applied in different frameworks; nevertheless such approach has scarcely been reported to predict the reaction behavior of trickle beds by means of diffusion-convection-reaction models. Here, we investigate a multi-fluid model solved with a CFD-based methodology to evaluate the overall performance of high-pressure trickle-bed reactor. A multiphase CFD model was developed to simulate the multiphase reactive flow on the catalytic wet oxidation of mimicked phenolic wastewaters. Since mesh aperture, time stepping strategy and the application of under-relaxation parameters play a major role on the final validation of the multiphase model, several computational runs on the detoxification of liquid pollutants have to be validated accordingly and performed at transient conditions to realize new reactive flow insights of multiphase flow environment.

3. Mathematical model

3.1. Governing multiphase flow equations

The mass conservation equation for each phase is expressed in Eq. (1).

$$\frac{\partial}{\partial t}(\alpha_q \rho_q) + \nabla \cdot (\alpha_q \rho_q \vec{u}_q) = 0. \quad (1)$$

Liquid and gas phases are assumed to share void space in proportion to their volumes leading to the unitary sum of volume fractions sum in the cells domain: $\alpha_L + \alpha_G = 1$. The momentum conservation equation for the phase q after averaging is written in Eq. (2) and the respective tensor in Eq. (3).

$$\frac{\partial}{\partial t}(\alpha_q \rho_q \vec{u}_q) + \nabla \cdot (\alpha_q \rho_q \vec{u}_q \vec{u}_q) = -\alpha_q \nabla p + \nabla \cdot \bar{\vec{\tau}}_q + \alpha_q \rho_q \vec{g} + \sum_{p=1}^n (\vec{R}_{pq} + \dot{m}_{pq} \vec{u}_{pq} - \dot{m}_{qp} \vec{u}_{qp}), \quad (2)$$

$$\bar{\vec{\tau}}_q = \alpha_q \mu_q (\nabla \vec{u}_q + \nabla \vec{u}_q^T) + \alpha_q \left(\lambda_q - \frac{2}{3} \mu_q \right) \nabla \cdot \vec{u}_q \vec{I}. \quad (3)$$

Here $\mu_q (\mu_q = \mu_{l,q} + \mu_{t,q})$ and λ_q are the shear and bulk viscosity of phase q . The interphase force, \vec{R}_{pq} , depends on the friction, pressure, cohesion, and other effects; it conforms to the conditions that $\vec{R}_{pq} = -\vec{R}_{qp}$ and $\vec{R}_{qq} = 0$ being possible to express a simple interaction term by Eq. (4):

$$\sum_{p=1}^n \vec{R}_{pq} = \sum_{p=1}^n K_{pq} (\vec{u}_p - \vec{u}_q), \quad (4)$$

where $K_{pq} = K_{qp}$ is the interphase momentum exchange coefficient.

3.2. Closure laws for gas-liquid-solid drag

The incomplete understanding of the governing physical laws in multiphase reactors plus the nonlinear coupled nature of the equations make the complete solution largely dependent in the mechanistic principles so that closure equations for gas-liquid-solid interactions integrated in the overall momentum balance equation are often approximations based on theoretical assumptions much in the same way as pressure drop in packed bed flow is often correlated using Ergun equation [11]. Taking into account the model of Attou and Ferschneider [12], the interphase coupling terms are expressed in terms of interstitial velocities and phase volume fractions for gas-liquid, gas-solid and liquid-solid momentum exchange forms as expressed in Eqs. (5)–(7)

$$K_{GL} = \alpha_G \left(\frac{E_1 \mu_G (1 - \alpha_G)^2}{\alpha_G^2 d_p^2} \left[\frac{\alpha_S}{1 - \alpha_G} \right]^{2/3} + \frac{E_2 \rho_G (u_G - u_L) (1 - \alpha_G)}{\alpha_G d_p} \left[\frac{\alpha_S}{1 - \alpha_G} \right]^{1/3} \right), \quad (5)$$

$$K_{GS} = \alpha_G \left(\frac{E_1 \mu_G (1 - \alpha_G)^2}{\alpha_G^2 d_p^2} \left[\frac{\alpha_S}{1 - \alpha_G} \right]^{2/3} + \frac{E_2 \rho_G u_G (1 - \alpha_G)}{\alpha_G d_p} \left[\frac{\alpha_S}{1 - \alpha_G} \right]^{1/3} \right), \quad (6)$$

$$K_{LS} = \alpha_L \left(\frac{E_1 \mu_L \alpha_S^2}{\alpha_L^2 d_p^2} + \frac{E_2 \rho_L u_G \alpha_S}{\alpha_L d_p} \right). \quad (7)$$

3.3. Enthalpy and species continuity equations

The reactor gas–liquid mass transfer coefficient was determined by the correlations proposed by Larachi and Cassanello [13] and the heat transfer coefficient was calculated according to the correlation developed by Boelhouwer et al. [14]. The conservation of energy in multiphase applications can be described by a separate enthalpy equation for each phase as expressed in Eq. (8).

$$\frac{\partial}{\partial t}(\alpha_q \rho_q h_q) + \nabla \cdot (\alpha_q \rho_q \vec{u}_q h_q) = -\alpha_q \frac{\partial p}{\partial t} + \bar{\tau}_q : \nabla \vec{u}_q - \nabla \cdot (k_{eff} \nabla T)_q + \sum_{p=1}^n (\dot{m}_{pq} h_{pq} - \dot{m}_{qp} h_{qp}) + S_{q,h}. \quad (8)$$

The species continuity equation is expressed in Eq. (9):

$$\frac{\partial \alpha_q \rho_q C_{q,i}}{\partial t} + \nabla \cdot (\alpha_q \rho_q u_q C_{q,i}) = \nabla \cdot (\alpha_q \rho_q D_{q,i} \nabla C_{q,i}) + \alpha_q \rho_q S_{q,i}. \quad (9)$$

3.4. Turbulence modeling

As the Reynolds numbers range is wide (min: 10, max: 2500), the multiphase k - ε model is used for turbulence modeling [15]. For incompressible flows, the turbulent liquid viscosity $\mu_{t,L}$ is given in Eq. (10).

$$\mu_{t,L} = \rho_L C_\mu \frac{k_L^2}{\varepsilon_L}. \quad (10)$$

Turbulence parameters are obtained from the prediction of the transport equations for the k_L , kinetic energy, and ε_L , dissipation energy, written in Eqs. (11) and (12), respectively.

$$\frac{\partial}{\partial t}(\rho_L \alpha_L k_L) + \nabla \cdot (\rho_L \alpha_L \vec{u}_L k_L) = \nabla \cdot \left(\alpha_L \frac{\mu_{t,L}}{\sigma_k} \nabla k_L \right) + \alpha_L G_{k,L} - \alpha_L \rho_L \varepsilon_L + \alpha_L \rho_L \Pi_{k,L}, \quad (11)$$

$$\frac{\partial}{\partial t}(\rho_L \alpha_L \varepsilon_L) + \nabla \cdot (\rho_L \alpha_L \vec{u}_L \varepsilon_L) = \nabla \cdot \left(\alpha_L \frac{\mu_{t,L}}{\sigma_\varepsilon} \nabla \varepsilon_L \right) + \alpha_L \frac{\varepsilon_L}{k_L} \times (C_{1\varepsilon} G_{k,L} + C_{2\varepsilon} \rho_L \varepsilon_L) + \alpha_L \rho_L \Pi_{\varepsilon,L}. \quad (12)$$

3.5. Simulation setup

The discretization of the governing equations was done by the finite-volume method as similarly described elsewhere [16]. A segregated implicit solver available in commercial CFD package FLUENT was employed to evaluate the resulting linear system of equations. The condition required for grid convergent results was based on a 1% relative error criterion and the simulations accuracy has been assessed by direct comparison with experimental data. The computational mesh representing the solid cylindrical catalyst of the trickle-bed reactor was created using the integrated solid modeling and meshing program GAMBIT as described elsewhere [17]. Having previously considered that the trickle-bed reactor was filled with 13 layers in which around 200 nonoverlapping spherical particles of 2 mm diameter were necessary for each axial layer, we had made use of parallel computing on 48 nodes to deal with high memory requirements that were necessary to cope with a single computing node. Here, the three dimensional simulations have been carried out on Linux cluster based on AMD64 Dual-Core 2.2 GHz processor. As a single node is concerned with 26 mm of computational domain, the remainder of the calculations has been carried out simultaneously on 47 nodes. This computed methodology enable us to operate on the principle that large chemical reaction engineering problems can be divided into smaller ones, which are then solved concurrently to mimic the factual dimensions of the experimental installation.

The CWAO kinetic parameters for the commercial catalyst N-140 were similarly derived to the work developed by Lopes et al. [18]. The right-hand side term of Eq. (9), $S_{i,q}$, include the reaction rates in terms of the total organic carbon concentration of the lumped species A , B and C as represented by Eq. (13).

$$\begin{aligned} -r_{TOC_A} &= -\frac{dC_{TOC_A}}{dt} = (k'_1 + k'_2)C_{TOC_A} \\ -r_{TOC_B} &= -\frac{dC_{TOC_B}}{dt} = k'_3 C_{TOC_B} - k'_2 C_{TOC_A}, \end{aligned} \quad (13)$$

where first order reactions were assumed for each mechanism step of the Generalized Kinetic Model. After integrating these equations a mathematical expression for TOC evolution is obtained in Eq. (14).

$$\frac{C_{TOC}}{C_{TOC_0}} = \frac{k'_2}{k'_1 + k'_2 - k'_3} e^{-k'_3 t} + \frac{k'_1 - k'_3}{k'_1 + k'_2 - k'_3} e^{-(k'_1 + k'_2)t}. \quad (14)$$

The activation energies and the pre-exponential factors were calculated by using the Arrhenius plot for the N-140 kinetic studies. These values were used in the corresponding expressions of the reaction rate constants k'_1 , k'_2 , k'_3 as functions of temperature, according to Arrhenius law as described in Eq. (15).

$$\begin{aligned} k'_1 &= 452 \cdot \exp\left(-\frac{3.121 \times 10^3}{T}\right) \text{ min}^{-1}; \\ k'_2 &= 28.1 \cdot \exp\left(-\frac{3.612 \times 10^3}{T}\right) \text{ min}^{-1}; \\ k'_3 &= 4.32 \times 10^6 \cdot \exp\left(-\frac{9.814 \times 10^3}{T}\right) \text{ min}^{-1}. \end{aligned} \quad (15)$$

Our case study is based on the kinetic studies performed with commercial and laboratory-made catalysts which have been carried out in batch mode operation. Several authors including the recent work developed by Manole et al. [19] indicated that data derived from continuous operation of downflow or upflow flooded-bed reactors exhibited a similar oxidation behavior to that observed in batch mode, despite very different liquid–solid ratios for the catalytic wet air oxidation of 4-hydroxybenzoic acid.

The inlet turbulence quantities such as turbulent kinetic energy and turbulent dissipation rate were specified based on FLUENT documentation. The turbulent kinetic energy (k) was estimated from turbulence intensity as expressed in Eq. (16).

$$k = \frac{3}{2} (uI)^2, \quad (16)$$

where I is the turbulence intensity being given by Eq. (17).

$$I = 0.16(Re_{dH})^{-1/8}. \quad (17)$$

The turbulent dissipation rate (ε) was estimated from the turbulent viscosity ratio as expressed by Eq. (18).

$$\varepsilon = \rho C_\mu \frac{k^2}{\mu} \left(\frac{\mu_t}{\mu}\right)^{-1}, \quad (18)$$

where C_μ is an empirical constant specified in the turbulence model (0.09). At 30 bar and 200 °C, the inlet turbulent kinetic energies for the liquid ($u_L = 0.0055$ m/s) and gas phase ($u_G = 0.020$ m/s) were 0.518 and 8.117 mm²/s², respectively, whereas the turbulent dissipation rates were 0.0654 and 2.934 mm²/s³.

The right-hand side source term of momentum balance equation (Eq. (2)) with the interphase momentum exchange coefficients (Eqs. (5)–(7)) were implemented in preliminary modeling studies in the UDF exclusively and uniquely to benchmark the multiphase flow model which now encompasses a direct simulation framework. Similarly, the heat and mass transfer rates were used to estimate as a first guess to $S_{q,h}$ and $S_{q,i}$ in Eqs. (8) and (9). In those preliminary studies, this first step allowed to close the multiphase flow constitutive equations in an ensemble averaged computational domain. Aiming to refine and to confer a universal approach, direct numerical simulations evolved from the interstitial CFD solver and dealt internally with the microscopic flow without relying anymore of those macroscopic scale closures. The relevant gas and liquid thermo-physical properties at $P = 30$ bar used in the CFD simulations are summarized in Table 1. In Eq. (8), S_h includes sources of enthalpy due to chemical reaction of phenolic compounds: -3000 kJ/mol [20]. Water properties, dissolved oxygen, phenolic compound diffusion coefficients, water and gas heat capacities, water heat of evaporation, heats of reaction, water vapor pressure and water density have been obtained from data or methods presented elsewhere [20]. Henry constants for oxygen solubility in water were taken from Himmelblau [21]. Phenolic compound and oxygen molecular diffusion coefficients have

Table 1
Relevant thermophysical properties of gas and liquid phases at $P = 30$ bar.

Properties	Value ($P = 30$ bar)		Units
	$T = 25$ °C	$T = 200$ °C	
<i>Liquid phase</i>			
Viscosity	8.925×10^{-4}	1.340×10^{-4}	Pa s
Density	998.4	866.9	kg/m ³
Surface tension	7.284×10^{-2}	3.770×10^{-2}	N/m
<i>Gas phase</i>			
Viscosity	1.845×10^{-5}	2.584×10^{-5}	Pa s
Density	35.67	21.97	kg/m ³

been also estimated by the methods of Wilke and Chang [22] and Siddiqi and Lucas [23]. Effective diffusion coefficient of pollutant in water and gaseous oxygen–solid mass transfer coefficients have been estimated from Piché et al. [24]. Phenolic compound liquid–solid mass transfer coefficient has been calculated from Goto and Smith [25] and gaseous oxygen–liquid volumetric mass transfer coefficient has been derived from Iliuta et al. [26].

Computations are time dependent and were performed until steady state conditions were reached. Standard wall functions were employed for turbulent flow conditions. The three dimensional simulations have been carried out on Linux cluster based on AMD64 Dual-Core 2.2 GHz processor. Although FLUENT documentation recommends a range of 30–50 for the cell thickness (y^+), in packed-bed flow it is almost impossible to meet the y^+ criterion everywhere on the sphere surface so that this value computed by the CFD solver was always below 200. The trickle-bed reactor studies have been carried out in pilot plant comprising a cylindrical reactor in stainless steel (SS-316) with 50 mm of internal diameter and 1.0 m length and the experimental procedure has been described elsewhere [27].

4. Results and discussion

4.1. Optimization of grid density

As trickling flow regime is described by different mechanisms of transport phenomena in zones either confined to the boundary layer or to the eventual large void spaces between catalyst particles, the solution method should be capable of accurately capturing sharp gradients in zones dominated by both convection and diffusion-related events. This task was accomplished to properly resolve zones with sharp gradients so extremely fine meshes were deployed in the vicinity of the walls. However, coarse meshes have been found to appropriately resolve convection-dominated zones involving small gradients. We started the parametric optimization of grid density to ensure mesh-independent solutions and since we found a wide range for the number of tetrahedral cells, one should also be aware that conventional numerical methods tend to be very inefficient as they necessitate quite uniform meshes for the entire computational domain. In order to cope with these numerical issues, several upwinding techniques were investigated in the field of finite volume methodology even if these techniques can generate higher numerical errors due to artificial diffusion and dispersion on dealing with numerical concerns on the local mesh-based Reynolds. Specifically, to address spatial and temporal variations of flow, reactants concentration and temperature within the trickle-bed reactor, a prevailing objective was to demonstrate the effectiveness of the current CFD framework coupling the heterogeneous nature of multiphase flow with the catalytic wet oxidation kinetics. The high-order monotonic upwind discretization scheme for conservation laws (MUSCL) has been employed both for the momentum balance equation and the continuity species conservation equation so as to avoid the “numerical diffusion” that arose during the CFD simulations giving the better compromise between numerical accuracy and computational expenditure. At this point, if one undertakes the velocity-mesh orthogonality condition, high-order differencing schemes perform well simply in case of computational domains where the flow velocity is aligned with the mesh. Unless stated otherwise, we extended the application of MUSCL in our three-dimensional case-study giving particular attention to the numerical accuracy. It should be pointed out that MUSCL and other high-order differencing schemes may be compromised significantly if irregular meshes are used to mimic complex geometries.

The computational grid is first refined in the flow direction to duplicate the total number of volumes that were present in the parent mesh. The parametric optimization was stopped if no deviations are found in concentration and temperature profiles compared to those obtained before the mesh refinement. Different mesh apertures were applied to refine the computational grid in eight levels: four levels for the coarser meshes with 2×10^5 , 6×10^5 , 1×10^6 , 1.4×10^6 of tetrahedral cells and four levels for the finer meshes with 1.8×10^6 , 2.2×10^6 , 2.6×10^6 and 3×10^6 of tetrahedral cells. Fig. 1 displays the influence of the number of tetrahedral cells on the total organic carbon concentration profile when the catalytic abatement of phenolic wastewaters was simulated at $L = 6 \text{ kg/m}^2 \text{ s}$, $G = 0.3 \text{ kg/m}^2 \text{ s}$ and $T = 200^\circ\text{C}$, $P = 30 \text{ bar}$. As can be seen from Fig. 1, the increase of mesh density led to an asymptotic solution as one increases the number of cells from 2.2×10^6 onwards. An incorrect computation of boundary layer at particle surface has been found by low mesh density characterized by 2×10^5 of tetrahedral cells. Providing the mesh density increases, the theoretical predictions of total organic carbon conversion improves remarkably. Indeed, as soon as the mesh is successively refined to give ca. tenfold the number of cells, the same performance is repeated confirming that the solutions obtained with the higher densities meaning that were already converged. However, a significant rise in computational time is reported which for the densest mesh is several hours. Depending on the hydrodynamic flow regime, the boundary conditions needed to enforce along the whole boundary or parts of the boundary enclosing the computational domain may be different for the numerical solution of governing differential equations. This is partly ascribed to the low interaction regime achieved between the gas and the liquid phase under trickling flow conditions. Here, it is anticipated for pulsing flow simulations that those boundary conditions emerge differently from the physics underlying the process. However, for the current results, the simulated variations of the field unknowns are not found to be perfectly symmetrical along the axis of domain parallel to the direction of flow. This fact may be attributed to the complex geometry which is not streamlined with the flow that characterized the packed bed flow environment.

In addition, several computational runs were performed changing the mesh density on the catalyst particle surface to accurately capture the boundary layer now on the temperature profile in what regards also the mesh sensitivity analysis. The effect of mesh aperture on the thermal behavior of the trickle-bed reactor is portrayed in Fig. 2 at $L = 6 \text{ kg/m}^2 \text{ s}$,

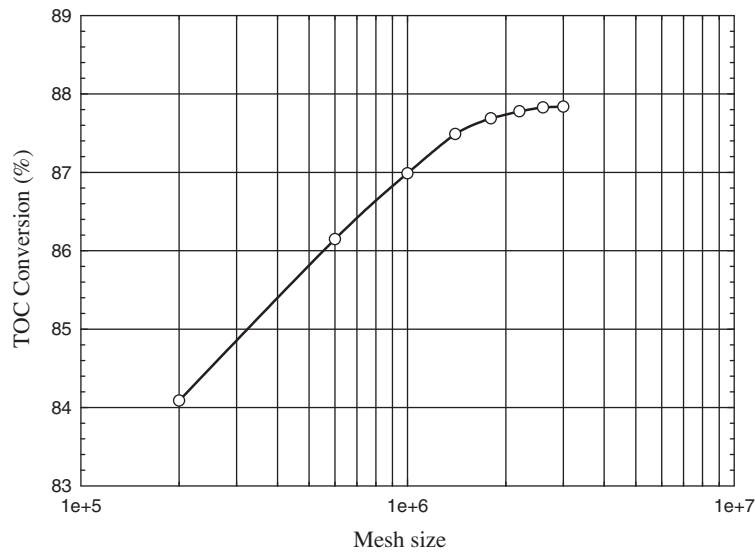


Fig. 1. Comparison of CFD predictions on normalized total organic carbon conversion for different mesh resolutions ($L = 6 \text{ kg/m}^2 \text{ s}$, $G = 0.3 \text{ kg/m}^2 \text{ s}$, $P = 30 \text{ bar}$, $d_p = 2 \text{ mm}$).

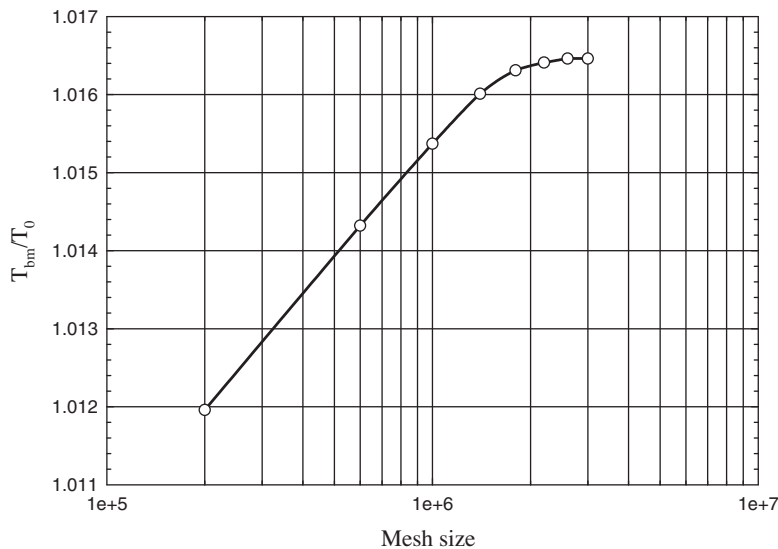


Fig. 2. Comparison of CFD predictions on normalized bulk temperature for different mesh resolutions ($L = 6 \text{ kg/m}^2 \text{ s}$, $G = 0.3 \text{ kg/m}^2 \text{ s}$, $P = 30 \text{ bar}$, $d_p = 2 \text{ mm}$).

$G = 0.3 \text{ kg/m}^2 \text{ s}$ and $T = 200^\circ \text{C}$, $P = 30 \text{ bar}$. Once again, the CFD predictions converged as soon as we used a computational grid comprising 2.2 million of tetrahedral cells. There is also an interesting fact revealed by Figs. 1 and 2, which is related to the monotony exhibited by the total organic carbon conversion and temperature profiles. As evidenced by the mesh sensitivity analysis, the asymptotic behavior of total organic carbon profile is monotonically increasing until the final conversion approaches the experimental value at steady-state. Likewise, the temperature profile is a monotonically increasing function as one increases the density of the computational grid. As long as the catalytic wet oxidation follows the Arrhenius's law, the higher conversions are accompanied with increasing values of the bulk phase temperature as exhibited by thermal profile in Fig. 2.

4.2. Time step sensitivity tests

Although steady diffusion–convection problems have been investigated extensively using non-upwinding methods, in our case-study the hydrodynamic regime is intrinsically dynamic so it was required efficient temporal discretization

schemes to deal with time-dependent frameworks under trickling flow conditions. Due to complexity of the interaction regime between the gas and liquid phases, the integration of multiphase governing equations over time and space was largely affected by the characteristic variations of boundary temperatures and heat fluxes as well as for the total organic carbon concentrations. Here, we have needed both temporal and spatial approximations for the accurate computation of such boundary zones so we will focus now on the temporal discretization of the governing flow equations. Having considered that higher-order time interpolation functions for transient mass and heat transfer coupled with the catalytic wet oxidation kinetics were deeply investigated for diffusion-related systems, one should also evaluate them for trickle beds where convection cannot be neglected.

According to the CFD-based simulations reported so far, all numerical implementations for the time-dependent diffusion–convection–reaction systems suggested that a more efficient numerical implementation regarding the time-stepping strategy was mandatory. During the CFD multiphase calculations, we employed first-order and second-order time discretization methods. This latter scheme was found to give confident computed results in comparison to the former one as long as the second-order time-accurate scheme achieves its accuracy by using an Euler backward approximation in time. This fact can in all likelihood be ascribed to the fully implicit methodology which highlighted an unconditional stability. A fair implementation of one of these methods for solving the scalar transport equation entails more than the time-stepping formula. Additionally, we have investigated the time step in the range: 10^{-5} , 10^{-4} , 10^{-3} and 10^{-2} s. Fig. 3 plots the CFD computations of total organic carbon conversions attained with those values at $L = 6 \text{ kg/m}^2 \text{ s}$, $G = 0.3 \text{ kg/m}^2 \text{ s}$ and $T = 200^\circ \text{C}$, $P = 30 \text{ bar}$. A similar asymptotic trend was depicted in Fig. 3 so we have identified a time step of 10^{-5} s which agreed better with the experimental data. Concomitantly, the analysis of the temperature profile obtained at $L = 6 \text{ kg/m}^2 \text{ s}$, $G = 0.3 \text{ kg/m}^2 \text{ s}$ and $T = 200^\circ \text{C}$, $P = 30 \text{ bar}$ reinforced the above-mentioned selection on the time step assessment, see Fig. 4. Once again, it is worth remarking the analogous behavior that described the total organic carbon conversion and temperature profiles illustrated in Figs. 3 and 4. The Arrhenius's temperature dependence of the rate constant for the catalytic wet oxidation is emphasizing hitherto on the monotonic nature of mesh density and time step profiles. We should emphasize that eventually on the pursuit of finer time resolution with higher computational grid densities, this fact would lead to impractical over-refined meshes and the efficiency of finite volume methodology decreases dramatically.

4.3. Convergence and stability

As mentioned before, the catalytic wet oxidation within the trickle-bed reactor involved the multi-component pollutant diffusion mainly due to the hydrodynamic interaction regime achieved under the present flow conditions. Conversely to for high mass transport Peclet number problems, the diffusion of both phenolic compounds and molecular oxygen cannot be neglected so we have constituted a diffusion–convection–reaction system of equations. These equations became tightly coupled through the nonlinear volumetric reaction source term. Provided that the computation of the reaction source is computationally expensive, one was motivated by the different reaction and heat/mass transport time scales to solve that system of equations in a segregated fashion. This methodology was accomplished at the first stage by the explicit computation of chemical reaction sources by time integration of the ordinary differential equations arising out of the catalytic wet oxidation kinetics. The calculated terms was then substituted into the multiphase flow constitutive equations, which are then solved in

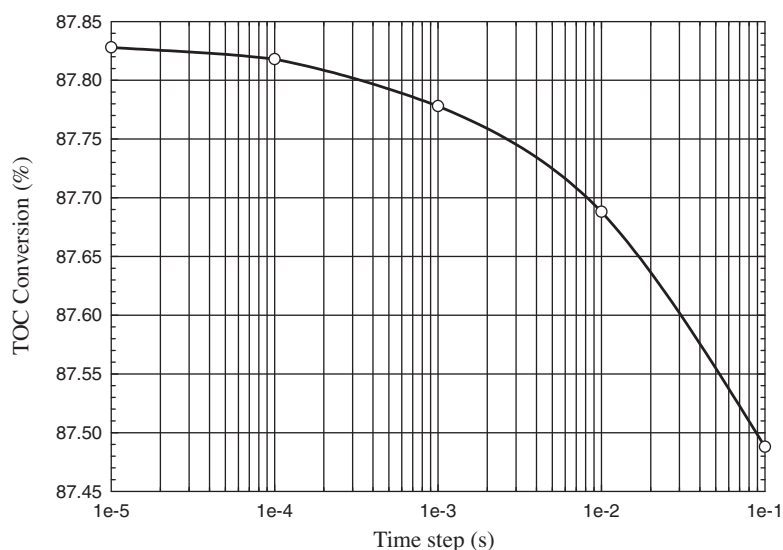


Fig. 3. Effect of time step on normalized total organic carbon conversion ($L = 6 \text{ kg/m}^2 \text{ s}$, $G = 0.3 \text{ kg/m}^2 \text{ s}$, $P = 30 \text{ bar}$, $d_p = 2 \text{ mm}$).

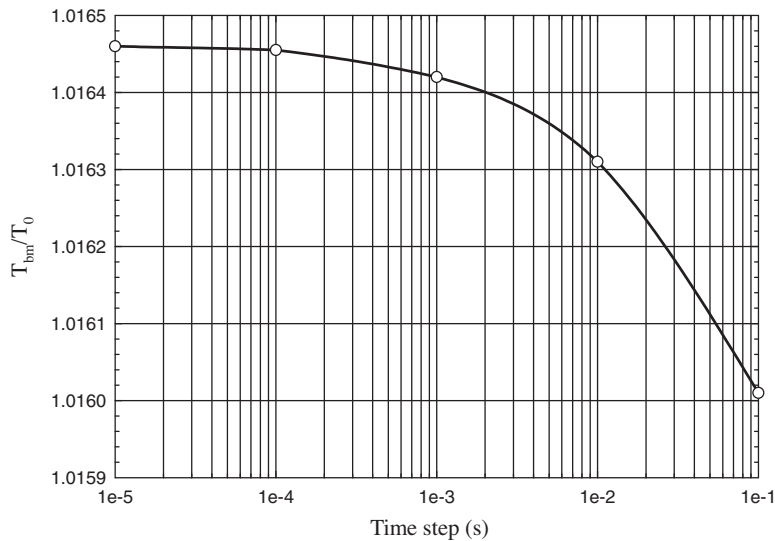


Fig. 4. Effect of time step on normalized bulk temperature ($L = 6 \text{ kg/m}^2 \text{ s}$, $G = 0.3 \text{ kg/m}^2 \text{ s}$, $P = 30 \text{ bar}$, $d_p = 2 \text{ mm}$).

sequential steps rather than simultaneously. Having labeled this mathematical algorithm as a segregated approach, the following rationale was to query the convergence and stability plots. The computed residuals were evaluated temporally during the examination of several mesh apertures and different time steps on the reaction properties.

The numerical integration based on the calculations made by the finite volume method led to the application of different under-relaxation parameters to deal efficiently with a stable computation of total organic carbon conversion and temperature profiles. The computational grid was typically characterized with 137 layers in which around 443 spherical particles of 2 mm diameter were necessary for each axial layer. According to the earlier discussions, if one uses 2.2×10^6 computational nodes for each layer, we needed approximately 3.01×10^8 nodes to obtain an asymptotic solution. As there are typically 9 unknowns at each node comprising 4 mass fractions, temperature, pressure, and 3 velocity components, the CFD calculations were performed with ca. 2.71×10^9 unknowns.

Fig. 5 shows the convergence plot obtained for various under-relaxation factors using segregated solution on the calculation of total organic carbon conversion at $L = 6 \text{ kg/m}^2 \text{ s}$, $G = 0.3 \text{ kg/m}^2 \text{ s}$ and $T = 200^\circ \text{C}$, $P = 30 \text{ bar}$. The accuracy and convergence of the model was investigated with 3 different under-relaxation factors: 0.6, 0.7, and 0.8. The higher the under-relaxation factor was, the worst convergence speed was obtained for the computation of TOC conversion with finite volume space discretization. The lowest-valued factor has revealed to be very effective on the numerical simulation of the

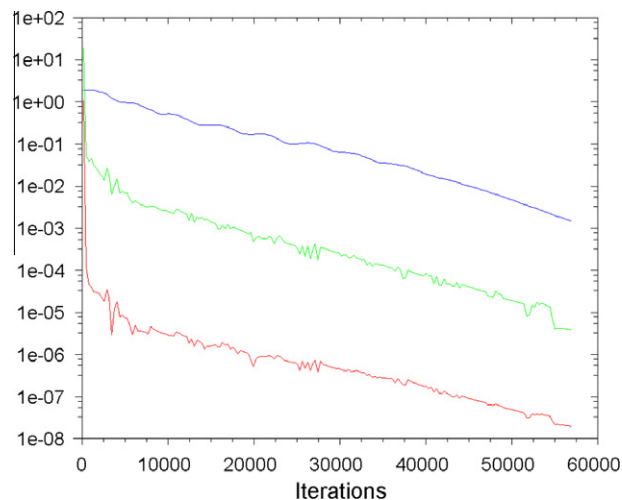


Fig. 5. Convergence plot of mean bulk total organic carbon conversion for various under-relaxation factors: red-0.6, green-0.7, blue-0.8 ($L = 6 \text{ kg/m}^2 \text{ s}$, $G = 0.3 \text{ kg/m}^2 \text{ s}$, $P = 30 \text{ bar}$, $d_p = 2 \text{ mm}$). (For interpretation of the references to colour in this figure legend, the reader is referred to the web version of this article.)

mineralization degree of liquid pollutants by catalytic wet oxidation. Fig. 6 illustrates the application of different under-relaxation factor on the computation of the temperature profile at $L = 6 \text{ kg/m}^2 \text{ s}$, $G = 0.3 \text{ kg/m}^2 \text{ s}$ and $T = 200^\circ\text{C}$, $P = 30 \text{ bar}$. Up to this point, one may advance that the mathematical behavior exhibited by Figs. 5 and 6 which was virtually similar can be related with the coupling level attained by the constitutive diffusion-convection-reaction equations. Guided by the parametric optimization already started, we have also evaluated the solver relaxation factors to control how far to advance the solution of the total organic carbon concentration and temperature fields. According to Figs. 5 and 6, if they were set too high the flow simulation will eventually diverge; notwithstanding, if they were set too low then the flow simulation required an excessive number of iterations to converge.

The convergence plot of total organic carbon conversion for three different mesh sizes: 1.8×10^6 , 2.2×10^6 , 2.6×10^6 is shown in Fig. 7 at $L = 6 \text{ kg/m}^2 \text{ s}$, $G = 0.3 \text{ kg/m}^2 \text{ s}$ and $T = 200^\circ\text{C}$, $P = 30 \text{ bar}$, whereas the convergence plot of temperature is depicted by Fig. 8 for the same computational grid densities. As can be seen from both convergence profiles, the results have exhibited numerical fluctuations from the first 10000 iterations onwards so to avoid these oscillations high-resolution discretization algorithm based on the MUSCL was found to be computationally attractive. The computed results were in good agreement with the experimental data and the comparison suggested that the transport phenomena in the trickle-bed reactor can be reliably predicted and easily understood compared to macroscopic reactor systems. From both convergence plots depicted by Figs. 7 and 8, robust convergence was observed, although it is somewhat quicker than the previous ones. As the

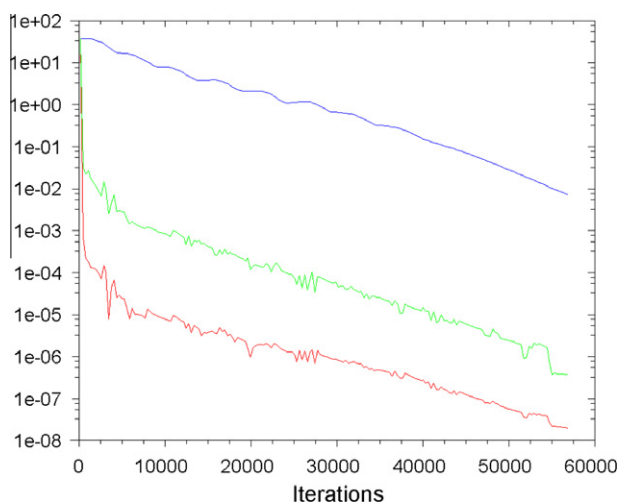


Fig. 6. Convergence plot of mean bulk temperature for various under-relaxation factors: red-0.6, green-0.7, blue-0.8 ($L = 6 \text{ kg/m}^2 \text{ s}$, $G = 0.3 \text{ kg/m}^2 \text{ s}$, $P = 30 \text{ bar}$, $d_p = 2 \text{ mm}$). (For interpretation of the references to colour in this figure legend, the reader is referred to the web version of this article.)

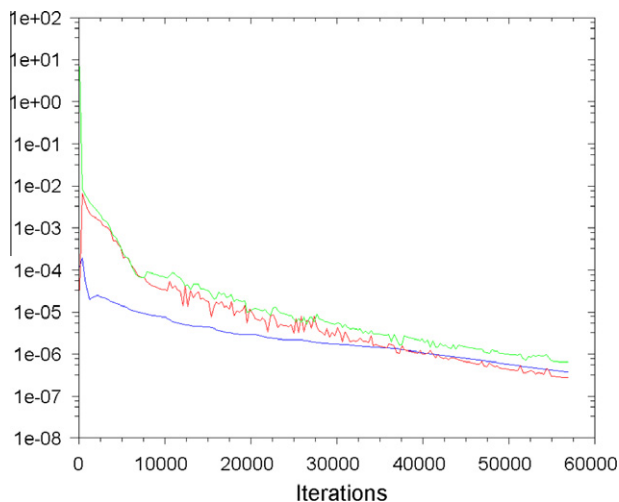


Fig. 7. Convergence plot of mean bulk total organic carbon conversion for various mesh sizes: red- 1.8×10^6 , green- 2.2×10^6 , blue- 2.6×10^6 ($L = 6 \text{ kg/m}^2 \text{ s}$, $G = 0.3 \text{ kg/m}^2 \text{ s}$, $P = 30 \text{ bar}$, $d_p = 2 \text{ mm}$). (For interpretation of the references to colour in this figure legend, the reader is referred to the web version of this article.)

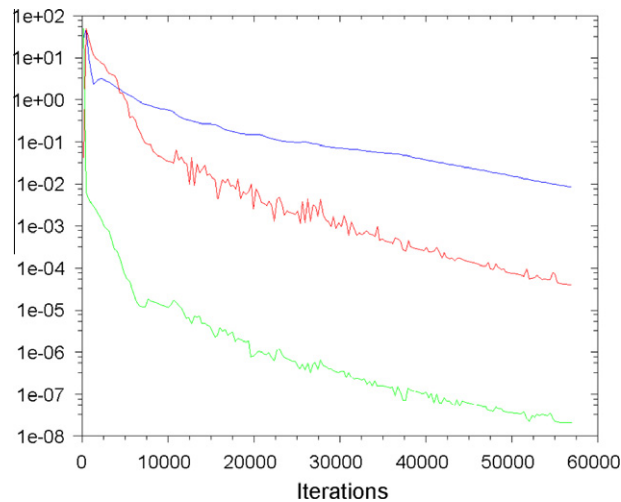


Fig. 8. Convergence plot of mean bulk temperature for various mesh sizes: red- 1.8×10^6 , green- 2.2×10^6 , blue- 2.6×10^6 ($L = 6 \text{ kg/m}^2 \text{ s}$, $G = 0.3 \text{ kg/m}^2 \text{ s}$, $P = 30 \text{ bar}$, $d_p = 2 \text{ mm}$). (For interpretation of the references to colour in this figure legend, the reader is referred to the web version of this article.)

numerical solution of the constitutive equations was stiff in temporal direction due to diffusive terms and steep in spatial direction due to convective terms, the CFD-based computations have exhibited this fact either investigating the reaction conversion or bulk temperature. In case of different numerical tuning parameters as confirmed by the effect of under-relaxation factors and mesh apertures, see Figs. 5–8, respectively, non-oscillatory and total variation diminishing methods improved remarkably the accuracy eliminating the numerical fluctuations at the expense of increased computational costs.

Fig. 9 and 10 illustrate the convergence plots of total organic carbon conversion and temperature, respectively, for different time steps in the range: 10^{-5} , 10^{-4} , and 10^{-3} s at $L = 6 \text{ kg/m}^2 \text{ s}$, $G = 0.3 \text{ kg/m}^2 \text{ s}$ and $T = 200^\circ \text{C}$, $P = 30 \text{ bar}$. As discussed above on the advection term, an improper choice of time stepping scheme may lead to unstable and oscillatory results and higher order time-stepping schemes were required. As can be seen in Figs. 9 and 10 considerable fluctuations were detected in the results confirming that apart from diffusion, convection should be also accounted for the transport of gas oxidant and liquid pollutants as well as energy. Nonetheless, the mass transport was not found to be dominated solely by convection so this issue was somewhat related with the timing studies required to evaluate steady state pollutant conversions under steady state.

4.4. Interstitial reactive flow

With all these parametric optimizations for the numerical solution variables, it was possible to evaluate interstitial reactive flow maps within the trickle-bed reactor. As long as the multiphase interstitial flow is strongly dictated by the gas and

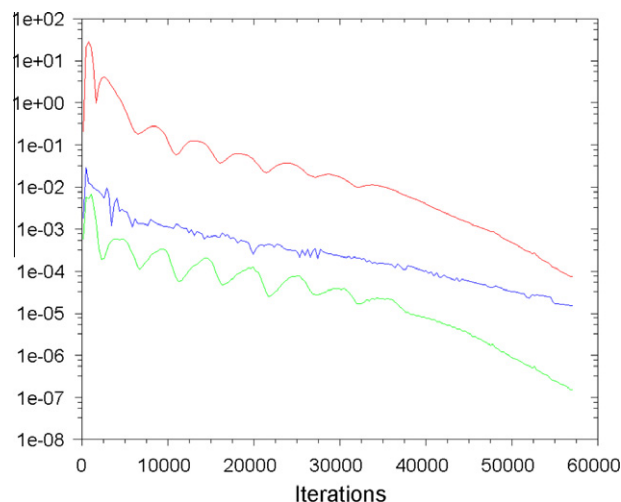


Fig. 9. Convergence plot of mean bulk total organic carbon conversion for various time steps: red- 10^{-3} s , green- 10^{-4} s , blue- 10^{-5} s ($L = 6 \text{ kg/m}^2 \text{ s}$, $G = 0.3 \text{ kg/m}^2 \text{ s}$, $P = 30 \text{ bar}$, $d_p = 2 \text{ mm}$). (For interpretation of the references to colour in this figure legend, the reader is referred to the web version of this article.)

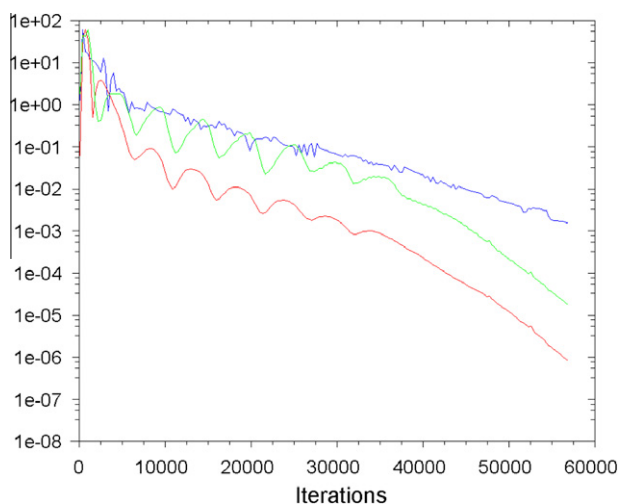


Fig. 10. Convergence plot of mean bulk temperature for various time steps: red- 10^{-3} s, green- 10^{-4} s, blue- 10^{-5} s ($L = 6 \text{ kg/m}^2 \text{ s}$, $G = 0.3 \text{ kg/m}^2 \text{ s}$, $P = 30 \text{ bar}$, $d_p = 2 \text{ mm}$). (For interpretation of the references to colour in this figure legend, the reader is referred to the web version of this article.)

liquid phase distribution different hydrodynamic regimes can be attained within the packed bed. Moreover, the velocity of the gas oxidant and the liquid pollutants can promote and increase the level of complexity at the time of proper scale-up. Steered by the past mechanistic modeling efforts on the hydrodynamic performance to give further insight to the inhomogeneity of gas–liquid reactive flow, here we analyse most importantly the total organic carbon and thermal profiles inside the multiphase reactor.

A semi-cylindrical slice made inside the catalytic bed is exhibited by Fig. 11 at $L = 6 \text{ kg/m}^2 \text{ s}$, $G = 0.3 \text{ kg/m}^2 \text{ s}$, $P = 30 \text{ bar}$, $T = 200^\circ\text{C}$ illustrating an instantaneous snapshot of liquid phase distribution colored by total organic carbon concentration, while Fig. 12 shows the same the instantaneous snapshot of liquid phase distribution colored by liquid temperature. These three-dimensional representations assisted by the multiphase model may shed some light on how small-scale details

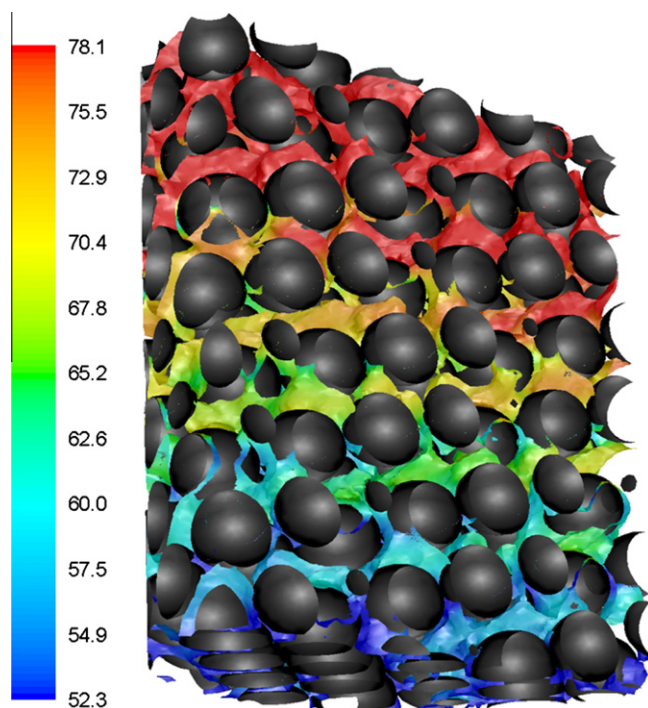


Fig. 11. Instantaneous snapshot of liquid phase distribution colored by total organic carbon concentration ($L = 6 \text{ kg/m}^2 \text{ s}$, $G = 0.3 \text{ kg/m}^2 \text{ s}$, $P = 30 \text{ bar}$, $T = 200^\circ\text{C}$, $d_p = 2 \text{ mm}$).

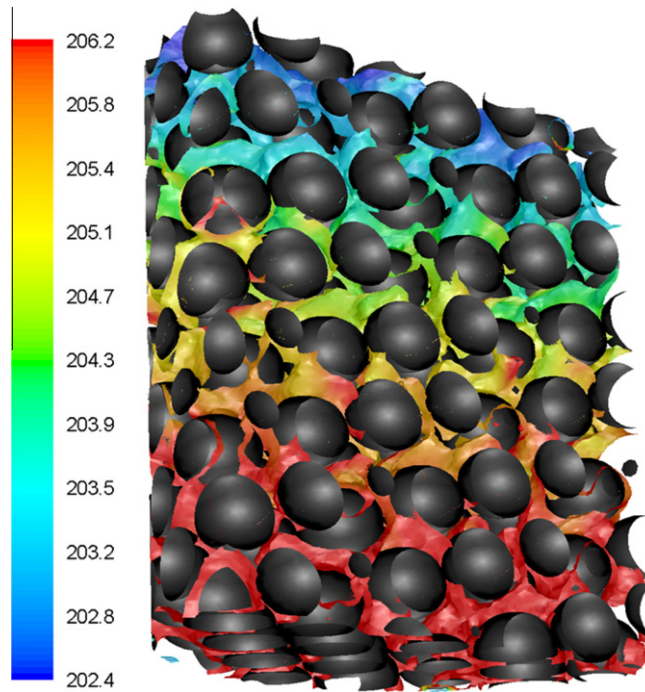


Fig. 12. Instantaneous snapshot of liquid phase distribution colored by liquid temperature ($L = 6 \text{ kg/m}^2 \text{ s}$, $G = 0.3 \text{ kg/m}^2 \text{ s}$, $P = 30 \text{ bar}$, $T = 200^\circ\text{C}$, $d_p = 2 \text{ mm}$).

actually dominate the trickle-bed reactor in much as the same way that tomographic imaging techniques attempt to provide information on phase fraction distribution and spatial mapping of chemical composition at high spatial and temporal resolution [28]. The multifaceted fluid texture depicted in Figs. 11 and 12 unveiled how the local liquid-catalyst contacting characteristics vary within the trickle bed, where it also was possible to identify the inter-particle space of the catalytic bed into

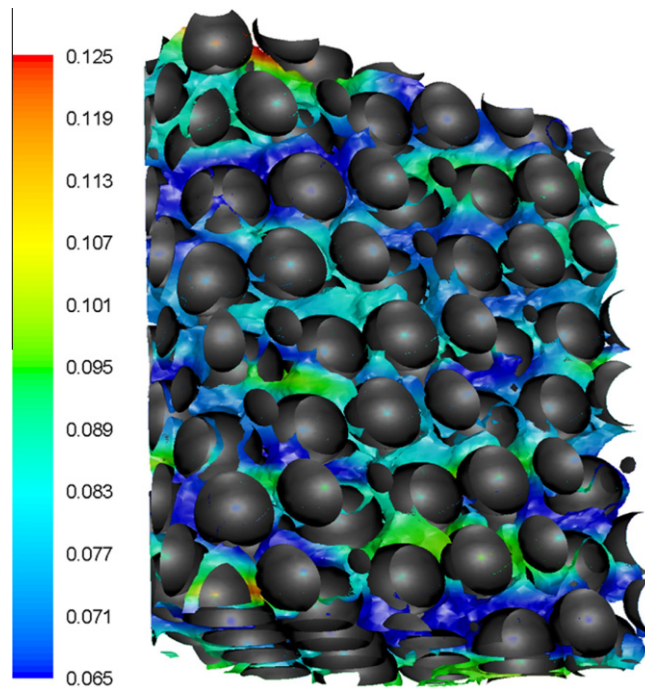


Fig. 13. Instantaneous snapshot of liquid phase distribution ($L = 6 \text{ kg/m}^2 \text{ s}$, $G = 0.3 \text{ kg/m}^2 \text{ s}$, $P = 30 \text{ bar}$, $T = 200^\circ\text{C}$, $d_p = 2 \text{ mm}$).

individual flow channels or the so-called pores. These events are illustrated by the instantaneous snapshots of liquid and gas phase distributions in Figs. 13 and 14, respectively. These gas–liquid channels are obtained in the three-dimensional representations and the spatial evolution of the local gas–liquid exhibited a liquid flow consisting of rivulets and films, the former exhibiting poor liquid–solid contacting regions and the latter being good liquid–solid contacting. These computational events have been experimentally observed by several authors on the rivulet/film categorization of gas–liquid distribution studies using computer-assisted tomography [29].

4.5. TOC and temperature simulation results

At $L = 6 \text{ kg/m}^2 \text{ s}$, $G = 0.3 \text{ kg/m}^2 \text{ s}$, $P = 30 \text{ bar}$, the CFD computations of total organic carbon conversion along the axial coordinate of trickle-bed reactor are shown with experimental data formerly (label: *non-optimized* – *n.o.*) and subsequently (label: *optimized* – *o.*) to the parametric optimization at different temperatures in Fig. 15. In the range 160–200 °C, five characteristic temperatures of catalytic wet oxidation have been used to query the effect of this reaction parameter on organic matter decontamination. As can be seen, conversion is favoured by increasing the temperature, hence we have the complete mineralization of organic matter after one half of reactor length when the simulation was carried out at the highest temperature (200 °C), see Fig. 15(e). However, none experimental measure on total organic carbon concentration has indicated that we have an absolute depletion of organic pollutants from the liquid phase. As can be seen from these concentration profiles, the parametric optimization unveiled a prominent role after evaluating the computed TOC results previously (label: *n.o.*) and subsequently (label: *o.*) to the multiphase reacting flow simulations. Examination of successive plots of Fig. 15 provides the ability to compare quantitatively CFD model predictions with the corresponding experimental conversion either through the averaged relative or absolute errors. At the lowest temperature ($T = 160 \text{ °C}$, see Fig. 15(a)), the averaged relative errors obtained at $z = 0.2, 0.4, 0.6, 0.8$ and 1 m were 4.2, 5.6, 7.1, 7.4 and 7.8%, respectively. Despite these values are remarkably increasing, the averaged absolute errors are decreasing and we had achieved 4.8, 3.4, 3.1, 2.7, 2.5 for $z = 0.2, 0.4, 0.6, 0.8$ and 1 m , respectively. In fact, the magnitude of the relative errors can be explained by the narrow range of TOC concentrations that were obtained at the reactor egress. At $z = 0.6$ and 0.8 m the TOC conversions were higher than 90% which produced very low concentration ratios $C_{\text{TOC}}/C_{\text{TOC0}}$ as illustrated in Fig. 15. Indeed, at $T = 170 \text{ °C}$ the averaged relative errors obtained with CFD model were 6.7, 7.6, 7.9, 8.1 and 8.9% for $z = 0.2, 0.4, 0.6, 0.8$ and 1 m whereas the averaged absolute errors were 5.4, 4.8, 4.3, 3.9, 3.6, respectively. Moreover, at the highest temperature the magnitude of the averaged relative errors was limited to 7.5, 8.1, 8.6, 8.7 and 8.8% albeit the averaged absolute errors kept almost the same intensity that was early identified at lower temperatures as 5.3, 4.9, 4.8, 3.9 and 3.5 for $z = 0.2, 0.4, 0.6, 0.8$ and 1 m , respectively.

Having considered all CFD computations at $L = 6 \text{ kg/m}^2 \text{ s}$, $G = 0.3 \text{ kg/m}^2 \text{ s}$, $P = 30 \text{ bar}$, one was able to identify the recurring underestimation of total organic carbon conversion for every simulated temperature if one did not parametrically optimized the numerical variables as described for the convergence and stability plots. Generally, it can be seen from Fig. 15 that com-

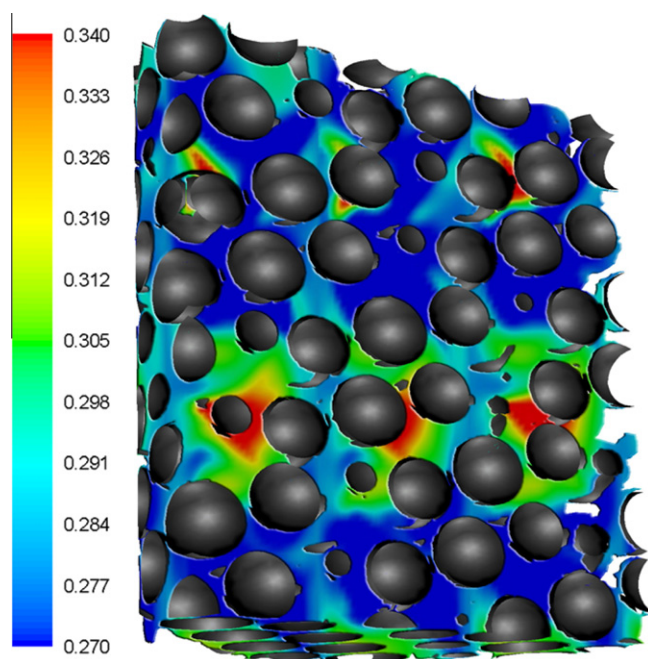


Fig. 14. Instantaneous snapshot of gas phase distribution ($L = 6 \text{ kg/m}^2 \text{ s}$, $G = 0.3 \text{ kg/m}^2 \text{ s}$, $P = 30 \text{ bar}$, $T = 200 \text{ °C}$, $d_p = 2 \text{ mm}$).

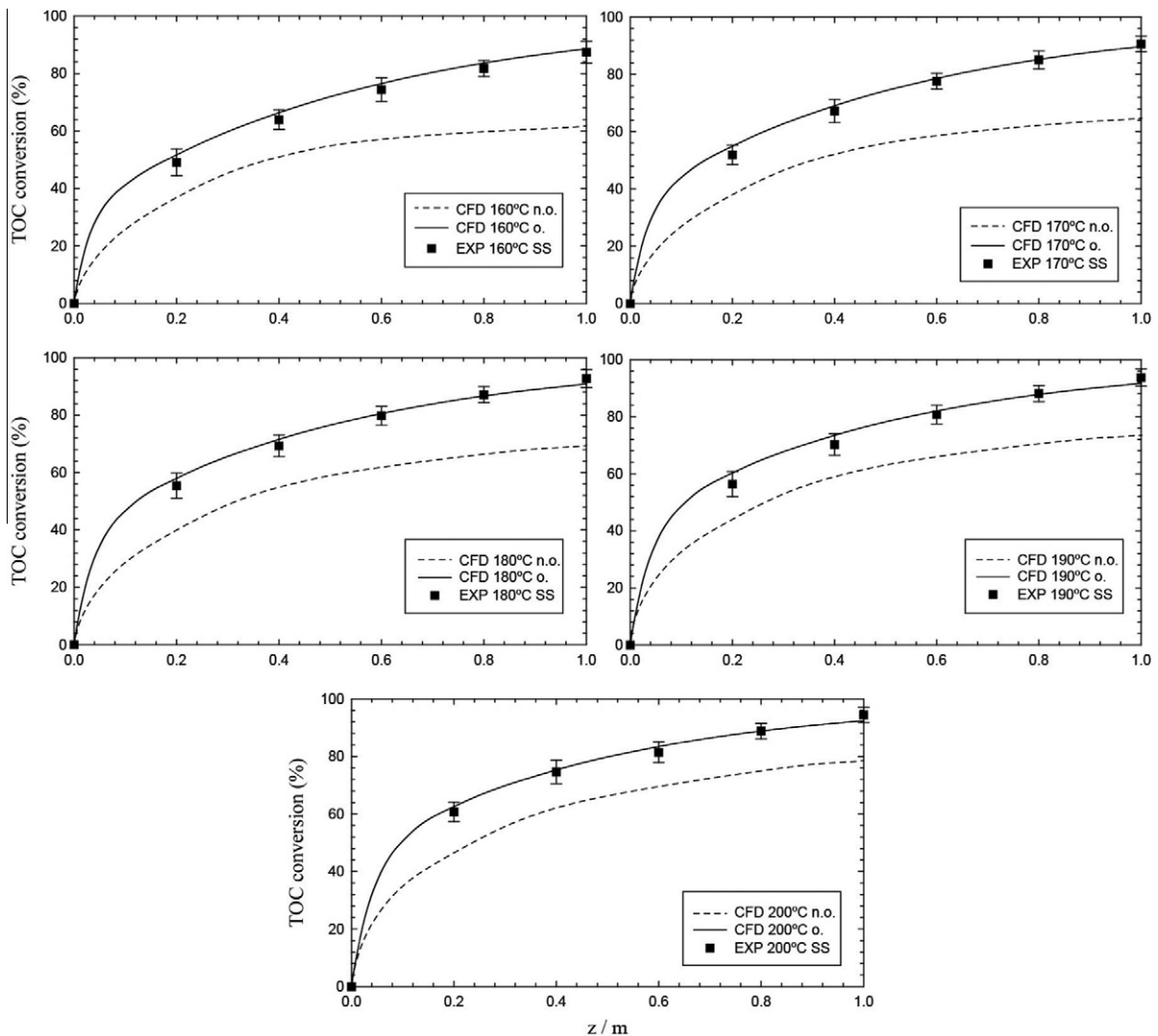


Fig. 15. Mean bulk total organic carbon conversion profiles for axial coordinate at different temperatures: non-optimized – n.o.; optimized – o. ($L = 6 \text{ kg/m}^2 \text{ s}$, $G = 0.3 \text{ kg/m}^2 \text{ s}$, $P = 30 \text{ bar}$, $d_p = 2 \text{ mm}$).

puted results agreed better with experimental data at the lower temperatures. This fact has been explained by the formulation of enthalpy balance meaning that a separate enthalpy equation for each phase in interstitial CFD models is more efficient on the prediction of temperature, which is used to compute the species concentration, against the shared formulation for enthalpy and temperature variables accounted by interface tracking models.

At $L = 6 \text{ kg/m}^2 \text{ s}$, $G = 0.3 \text{ kg/m}^2 \text{ s}$, $P = 30 \text{ bar}$, the averaged axial temperature profiles are depicted by Fig. 16. The thermal behavior exhibited by the trickle-bed reactor is a distinguishing feature of exothermic reactions. As long as the catalytic wet air oxidation of phenolic pollutants releases energy available from the lower enthalpy of reaction products in comparison to the higher enthalpy of reactants, the chemical conversion of those compounds into water and carbon dioxide is responsible by the temperature increase of bulk phase. This fact led to the heating of catalyst particles more pronounced in the first one fourth of trickle-bed length as portrayed in the thermal profiles of Fig. 16. The higher the inlet temperature was the stronger the increase of bulk phase temperature was attained at steady-state. The averaged relative errors at the lowest temperature were -2.1 , -0.9 , -0.7 , -0.6 and -0.6% for $z = 0.2, 0.4, 0.6, 0.8$ and 1 m , respectively. These averaged relative errors were almost identical to the ones obtained at $T = 170^\circ\text{C}$ and they have become lower when the catalytic wet oxidation was performed at the highest temperature giving -1.8 , -0.8 , -0.6 , -0.5 , and -0.4% for $z = 0.2, 0.4, 0.6, 0.8$ and 1 m , respectively. Bearing in mind this quantitative analysis, it can be argued that the interstitial CFD computations of total organic carbon conversion agreed better with experimental data at lower temperatures, whereas the computed CFD predictions of temperature profiles managed better at elevated temperatures.

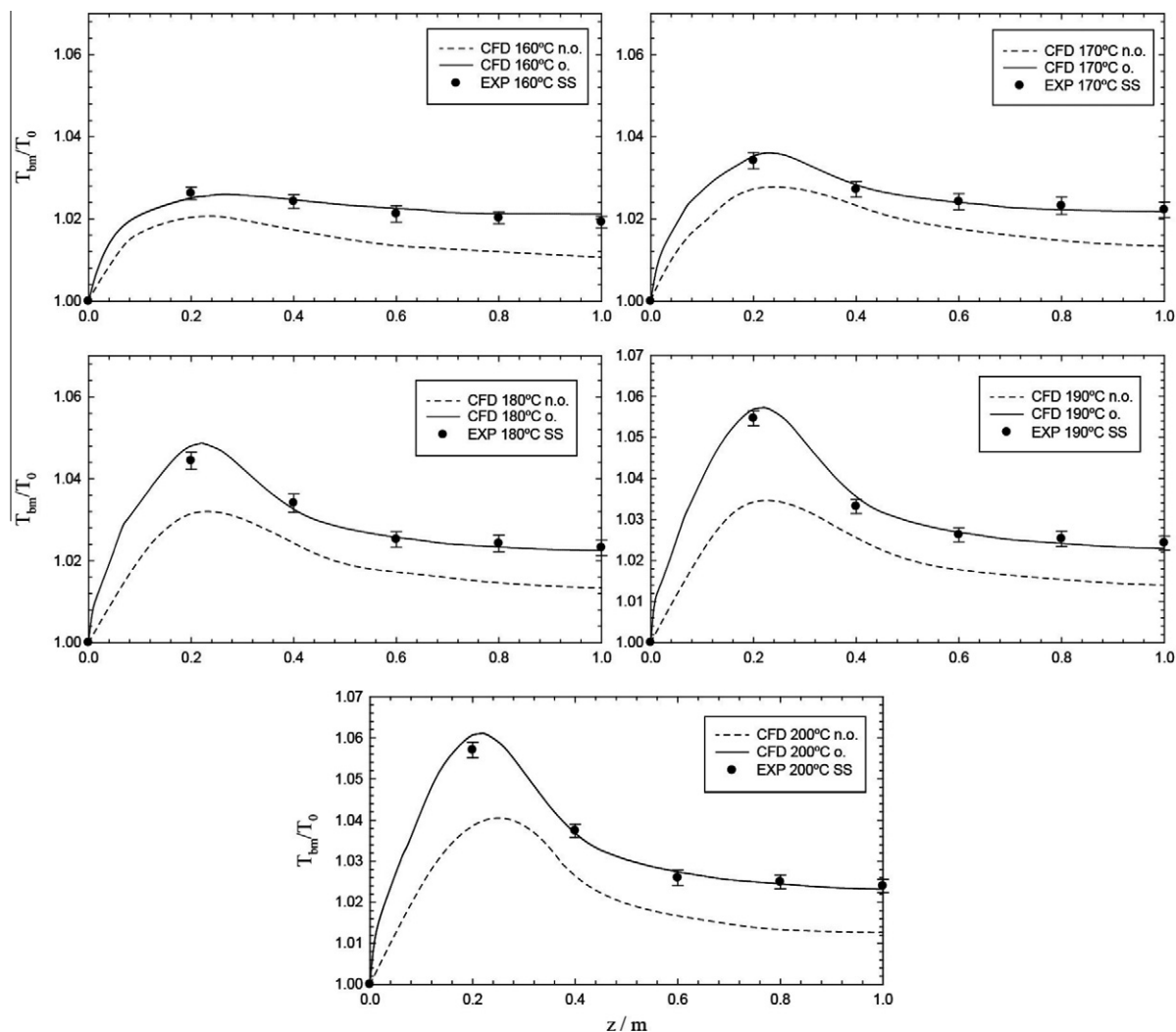


Fig. 16. Mean bulk temperature profiles for axial coordinate at different temperatures: non-optimized – n.o.; optimized – o. ($L = 6 \text{ kg/m}^2 \text{ s}$, $G = 0.3 \text{ kg/m}^2 \text{ s}$, $P = 30 \text{ bar}$, $d_p = 2 \text{ mm}$).

5. Conclusions

A comprehensive CFD model based on the conservative unstructured finite volume methodology has been investigated to bring new insights into gas–liquid–solid catalytic wet oxidation. The multiphase model accounted for hydrodynamics such as phase holdup, pressure drop, and liquid distribution apart from heat and mass transfer parameters. First, the heterogeneous flow constitutive equations of the trickle bed system have been derived by means of diffusion–convection–reaction model coupled within an interstitial framework. Second, as long as the application of under-relaxation parameters, mesh density, and time stepping strategy play a major role on the final validation, several computational runs on the detoxification of liquid pollutants were validated accordingly and evaluated in terms of convergence and stability criteria. Finally, the analysis of computational interstitial flow mappings for the reaction properties enabled the identification of relevant dry zones when the trickle-bed reactor was to be operated under trickling flow conditions.

Acknowledgment

The authors gratefully acknowledged the financial support of *Fundação para a Ciência e Tecnologia*, Portugal.

References

- [1] S.K. Bhargava, J. Tardio, J. Prasad, K. Fogar, D.B. Akolekar, S.C. Grocott, Wet oxidation and catalytic wet oxidation, *Ind. Eng. Chem. Res.* 45 (2006) 1221–1258.

- [2] M.P. Dudukovic, F. Larachi, P.L. Mills, Multiphase reactors—revisited, *Chem. Eng. Sci.* 54 (1999) 1975–1995.
- [3] M.R. Khadilkar, M.H. Al-Dahhan, M.P. Dudukovic, Multicomponent flow-transport-reaction modeling of trickle bed reactors: application to unsteady state liquid flow modulation, *Ind. Eng. Chem. Res.* 44 (2005) 6354–6370.
- [4] J. Guo, Y. Jiang, M.H. Al-Dahhan, Modeling of trickle-bed reactors with exothermic reactions using cell network approach, *Chem. Eng. Sci.* 63 (2008) 751–764.
- [5] M.K. Patel, N.C. Markatos, M. Cross, Method of reducing false-diffusion errors in convection–diffusion problems, *Appl. Math. Model.* 9 (1985) 302–306.
- [6] B.P. Leonard, Order of accuracy of QUICK and related convection–diffusion schemes, *Appl. Math. Model.* 19 (1995) 640–653.
- [7] S.J. DeSilva, C.L. Chan, A. Chandra, J. Lim, Boundary element method analysis for the transient conduction–convection in 2-D with spatially variable convective velocity, *Appl. Math. Model.* 22 (1998) 81–112.
- [8] J.M. Zhan, Y.Y. Luo, Y.S. Li, A high accuracy hybrid method for two-dimensional Navier–Stokes equations, *Appl. Math. Model.* 32 (2008) 873–888.
- [9] S. Korotov, Global a posteriori error estimates for convection–reaction–diffusion problems, *Appl. Math. Model.* 32 (2008) 1579–1586.
- [10] A. Mohebbi, M. Dehghan, High-order compact solution of the one-dimensional heat and advection–diffusion equations, *Appl. Math. Model.* 34 (2010) 3071–3084.
- [11] M.H. Al-Dahhan, F. Larachi, M.P. Dudukovic, A. Laurent, High pressure trickle-bed reactors: a review, *Ind. Eng. Chem. Res.* 36 (1997) 3292–3314.
- [12] A. Attou, G.A. Ferschneider, Two-fluid model for flow regime transition in gas–liquid trickle-bed reactors, *Chem. Eng. Sci.* 54 (1999) 5031–5037.
- [13] F. Larachi, M. Cassanello, A. Laurent, Gas–liquid interfacial mass transfer in trickle-bed reactors at elevated pressures, *Ind. Eng. Chem. Res.* 37 (1998) 718–733.
- [14] J.G. Boelhouwer, H.W. Piepers, A.A.H. Drinkenburg, Particle–liquid heat transfer in trickle-bed reactors, *Chem. Eng. Sci.* 56 (2001) 1181–1187.
- [15] S. Elghobashi, T. Abou-Arab, M. Rizk, A. Mostafa, Prediction of the particle-laden jet with a two-equation turbulence model, *Int. J. Multiphase Flow* 10 (1984) 697–710.
- [16] R.J.G. Lopes, R.M. Quinta-Ferreira, Turbulence modeling of high-pressure trickle-bed reactor, *Chem. Eng. Sci.* 64 (2009) 1806–1819.
- [17] R.J.G. Lopes, R.M. Quinta-Ferreira, CFD modeling of multiphase flow distribution in trickle beds, *Chem. Eng. J.* 147 (2009) 342–355.
- [18] R.J.G. Lopes, A.M.T. Silva, R.M. Quinta-Ferreira, Screening of catalysts and effect of temperature for kinetic degradation studies of aromatic compounds during wet oxidation, *Appl. Catal. B* 73 (2007) 193–202.
- [19] C.C. Manole, C. Julcour-Lebigue, A.M. Wilhelm, H. Delmas, Catalytic oxidation of 4-hydroxybenzoic acid on activated carbon in batch autoclave and fixed-bed reactors, *Ind. Eng. Chem. Res.* 46 (2007) 8388–8396.
- [20] R.C. Reid, J.M. Prausnitz, B.E. Poling, *The Properties of Gases and Liquids*, Mc-Graw-Hill, New York, 1987.
- [21] D.M. Himmelblau, Solubilities of inert gases in water. 0 °C to near the critical point of water, *J. Chem. Eng. Data* 5 (1960) 10–15.
- [22] C.R. Wilke, P. Chang, Correlation of diffusion coefficients in dilute solutions, *AIChE J.* 1 (1955) 264–270.
- [23] M.A. Siddiqi, K. Lucas, Correlations for prediction of diffusion in liquid, *Can. J. Chem. Eng.* 64 (1986) 839–843.
- [24] S. Piché, F. Larachi, I. Iliuta, B.P.A. Grandjean, Improving the prediction of liquid back-mixing in trickle-bed reactors using a neural network approach, *J. Chem. Technol. Biotechnol.* 77 (2002) 989–998.
- [25] S. Goto, J.M. Smith, Trickle bed reactors performance: I hold-up and mass transfer effects, *AIChE J.* 21 (1975) 706–713.
- [26] I. Iliuta, F. Larachi, B.P.A. Grandjean, G. Wild, Gas–liquid interfacial mass transfer in trickle-bed reactors: state-of-the-art correlations, *Chem. Eng. Sci.* 54 (1999) 5633–5645.
- [27] R.J.G. Lopes, R.M. Quinta-Ferreira, Assessment of CFD Euler–Euler method for trickle-bed reactor modeling in the catalytic wet oxidation of phenolic wastewaters, *Chem. Eng. J.* 160 (2010) 293–301.
- [28] P.G. Lutran, K.M. Ng, E.P. Delikat, Liquid distribution in trickle-beds. An experimental study using computer-assisted tomography, *Ind. Eng. Chem. Res.* 30 (1991) 1270–1280.
- [29] P.V. Ravindra, D.P. Rao, M.S. Rao, Liquid flow texture in trickle-bed reactors: an experimental study, *Ind. Eng. Chem. Res.* 36 (1997) 5133–5145.